Received: 13 December 2020 | Revised: 13 May 2021 | Accepted: 29 May 2021

DOI: 10.1002/fld.5017

RESEARCH ARTICLE

WILEY

A mass and momentum-conservative semi-implicit finite volume scheme for complex non-hydrostatic free surface flows

Davide Ferrari | **Michael Dumbser**

Laboratory of Applied Mathematics, University of Trento, Trento, Italy

Correspondence
Michael Dumbser, Laboratory of Applied Mathematics, University of Trento, Via Mesiano 77, 38123 Trento, TN, Italy.
Email: michael.dumbser@unitn.it

Funding information
Ministero dell'Istruzione, dell'Università e della Ricerca, Grant/Award Number: PRIN 2017

Abstract

In this article, a novel mass and momentum conservative semi-implicit method is presented for the numerical solution of the incompressible free-surface Navier–Stokes equations. This method can be seen as an extension of the semi-implicit mass-conservative scheme presented by Casulli. The domain is covered by the fluid, by potential solid obstacles, and by the surrounding void via a scalar volume fraction function for each phase, according to the so-called diffuse interface approach. The semi-implicit finite volume discretization of the mass and momentum equations leads to a mildly nonlinear system for the pressure. The nonlinearity on the diagonal of the system stems from the nonlinear definition of the volume, while the remaining linear part of the pressure system is symmetric and at least positive semi-definite. Hence, the pressure can be efficiently obtained with the family of nested Newton-type techniques recently introduced and analyzed by Brugnano and Casulli. The time step size is only limited by the flow speed and eventually by the velocity of moving rigid obstacles contained in the computational domain, and not by the gravity wave speed. Therefore, the method is efficient also for low Froude number flows. Moreover the scheme is formulated to be locally and globally conservative: for this reason it fits well in the presence of shock waves, too. In the special case of only one grid cell in vertical direction, the proposed scheme automatically reduces to a mass and momentum conservative discretization of the shallow water equations. The proposed method is first validated against the exact solution of a set of one-dimensional Riemann problems for inviscid flows. Then, some computational results are shown for non-hydrostatic flow problems and for a simple fluid-structure interaction problem.

KEYWORDS

free surface, Navier–Stokes, non-hydrostatic flows, piecewise linear system, staggered semi-implicit finite volume method

1 | INTRODUCTION

The method presented in this article is a momentum-conservative extension of the semi-implicit mass-conservative scheme for complex non-hydrostatic free surface flows presented by Casulli.[1] While in the previous publication, the momentum equation was written in primitive variables; in this article, a fully conservative form of the governing equations is used.

Nowadays, numerical modeling of free-surface hydrodynamics is widespread in environmental engineering applications; for example, in the simulation of water flow in rivers, lakes, and oceans or for the modeling of atmospheric flows. The governing equations for all these different applications can be derived from the laws of conservation of mass, momentum, and energy, leading to the so-called Navier–Stokes equations. These equations can be expressed in terms of *conserved variables* or *primitive variables*; still, using the first ones the equations are physically based on conservation laws and there are also some advantages from the numerical point of view.

The major difference between the various applications is the *Mach number* $M = ||v||/c$, which is the ratio between the flow velocity v and the sound speed c. While typical atmospheric flows present moderate Mach numbers, geophysical or in general natural water flows present very low Mach numbers. It can be shown[2] that when the Mach number tends to zero the compressible Navier–Stokes equations converge to the incompressible Navier–Stokes equations, thus leading, from the conservation of energy, to the divergence-free condition for the velocity. In that limit, the hydrodynamic pressure fluctuations are governed by an elliptic pressure Poisson equation, which keeps the velocity field divergence-free. Numerical schemes for low Mach number flows and incompressible flows are usually based on staggered meshes. For an overview that does not pretend to be complete, see, for example, References 3-15 and references therein.

In most environmental applications, these equations are further simplified. In fact, with large spatial scales, the vertical accelerations as well as the viscosity forces are small when compared to the gravity acceleration and to the pressure gradient in the vertical direction. Consequently, by neglecting the advective and the viscous term in the third momentum equation, the equation yields the hydrostatic pressure. These simplified equation describes three-dimensional hydrostatic flows and solving this system is much more convenient than solving the original Navier–Stokes equations. However, this hypothesis becomes less and less verified as the spatial scale decreases and becomes wrong when complex free-surface dynamics are coupled with structure interaction. In order to consider weakly non-hydrostatic effects in geophysical free surface flows, very frequently dispersive shallow water models are employed. For such non-hydrostatic dispersive shallow water models and their numerical discretization, the reader is referred, for example, to References 16-27.

The main aim of this article is to provide a novel pressure-based semi-implicit method for the incompressible free surface Navier–Stokes equations, which can deal with embedded solid structures a complex free surface topologies that are not limited to a single-valued function. Furthermore, the method is locally and globally conservative and its time step is only limited by the flow and structures velocities instead of the gravity wave speed. In the proposed scheme, the density equation is integrated to obtain an implicit finite volume discretization, and the nonlinear convective terms for momentum equation are discretized explicitly, while the pressure in the momentum equation is taken implicitly. This removes the stability condition on the gravity (pressure) wave speed and requires only a mild restriction of the time step based on the velocity of the fluid and the moving solid bodies. Then, the discrete momentum equation is inserted into the finite volume discretization of the mass conservation equation, leading to a mildly nonlinear system for the pressure. The diagonal nonlinearity of this system stems from the definition of volume of fluid, while the remaining linear part of the system is symmetric and at least positive semi-definite. Hence, the pressure can be efficiently obtained with the family of nested Newton-type techniques recently introduced and analyzed by Brugnano and Casulli.[28,29] The nonlinear volume function yields a diffuse interface formulation that allows to treat complex free surface topologies with almost arbitrary shape. For an overview of diffuse interface methods, see, for example, References 30-36 and references therein.

The rest of this article is organized as follows: in Section 2, the governing differential equations and the new numerical methods are presented; a thorough validation of one-dimensional inviscid flows is presented in Section 3; besides, some computational results for non-hydrostatic and for some simple flows around a rigid solid obstacle are also shown in this chapter. Finally, in Section 4, some concluding remarks are given.

2 | GOVERNING EQUATIONS AND NUMERICAL METHOD

2.1 | Governing PDE

For simplicity, but without losing any generality, a two-dimensional incompressible free-surface flow is considered on a simple rectangular computational domain. The extension to the three-dimensional case can be achieved by including variability in a second horizontal direction with an additional momentum equation.

The governing differential equations are the incompressible Navier–Stokes equations. Introducing the volume fraction α and assuming the density as a constant $\rho = const$, within a Cartesian coordinate system (x, y) where the x-axis is horizontal and the vertical y-axis is oriented upward along the gravity direction, the governing equations are given by

$$\begin{aligned} &\alpha_t + (\alpha u)_x + (\alpha v)_y = 0, \\ &(\alpha u)_t + (u\alpha u)_x + (v\alpha u)_y = -\alpha p_x + \alpha\nu(u_{xx} + u_{yy}), \\ &(\alpha v)_t + (u\alpha v)_x + (v\alpha v)_y = -\alpha p_y + \alpha\nu(v_{xx} + v_{yy}) - \alpha g, \end{aligned} \tag{1}$$

where $u(x, y, t)$ and $v(x, y, t)$ are the velocity components in the horizontal x and vertical z directions, t is the time, $p(x, y, t)$ is the normalized pressure with respect to the constant density, g is the gravity acceleration, $\nu = \mu/\rho$ is the kinematic viscosity coefficient, and the volume fraction α is related to the volume V occupied by the liquid in a control volume Ω_i by

$$V = \int_{\Omega_i} \alpha(x, y, t) dy dx. \tag{2}$$

2.2 | Computational grid and constitutive relationship

In order to solve the system (1) numerically in a fixed spatial domain $\Omega \subset \mathbb{R}^2$, a *staggered* grid is introduced. This grid consists of rectangular control volumes $\Omega_{i,j} = [x_{i-\frac{1}{2}}, x_{i+\frac{1}{2}}] \times [y_{j-\frac{1}{2}}, y_{j+\frac{1}{2}}]$ with barycenters in (x_i, y_j) and having width $\Delta x_i = x_{i+\frac{1}{2}} - x_{i-\frac{1}{2}}$ and height $\Delta y_j = y_{j+\frac{1}{2}} - y_{j-\frac{1}{2}}$. The discrete flow variables u, v, and p at time level t^n are defined at staggered locations as represented in Figure 1. The discrete pressure $p^n_{i,j}$ is defined in the centers of the cells $\Omega_{i,j}$, the velocity $u^n_{i\pm\frac{1}{2},j}$ is located at the center of each vertical edge, and the vertical velocities $v^n_{i,j\pm\frac{1}{2}}$ are defined at the center of each horizontal edge. The fluid velocities are assumed to be constant along their respective edges, whereas pressure has variability in the gravity direction. In particular, the pressure is assumed to be linear and hydrostatic within each cell with respect to the value in the center:

$$p(x, y, t^n) = p^n_{i,j} + g(y_j - y), \quad \forall (x, y) \in \Omega_{i,j}. \tag{3}$$

Furthermore, according to Reference 1 the volume of fluid within the cell $\Omega_{i,j}$ is related to the local cell pressure by the following *constitutive relationship*, which is more conveniently expressed in terms of a Jordan decomposition as

$$V^n_{i,j} = V(p^n_{i,j}) = P(p^n_{i,j})(p^n_{i,j} - \beta) - Q(p^n_{i,j})(p^n_{i,j} - \beta), \tag{4}$$

where $\beta = g\frac{\Delta y}{2}$, and P and Q are step functions defined as

$$P(p^n_{i,j}) = \begin{cases} \left(1 - \alpha^s_{i,j}\right)\frac{\Delta x}{g} & \text{if } p^n_{i,j} \geqslant -\beta, \\ 0 & \text{otherwise} \end{cases} \quad \text{and} \quad Q(p^n_{i,j}) = \begin{cases} \left(1 - \alpha^s_{i,j}\right)\frac{\Delta x}{g} & \text{if } p^n_{i,j} > \beta, \\ 0 & \text{otherwise.} \end{cases} \tag{5}$$

Here, $\alpha^s_{i,j}$ is the volume fraction of a potential solid obstacle contained in the cell i, j. For $\alpha^s_{i,j} = 1$, the corresponding cell obviously cannot be occupied by the liquid. Thus, as illustrated in Figure 2, the fluid volume is defined, for each cell, as a piecewise linear function of the local cell centered pressure. Finally, one also needs to define how to evaluate the edge

FIGURE 1 Discrete flow variables on a staggered grid

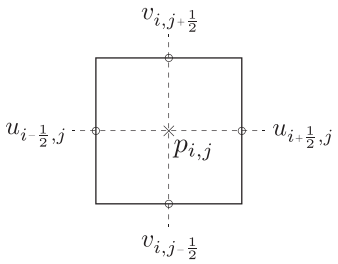

FIGURE 2 Fluid volume defined as a piecewise linear function of the local cell pressure in absence of any solid obstacle ($\alpha^s = 0$)

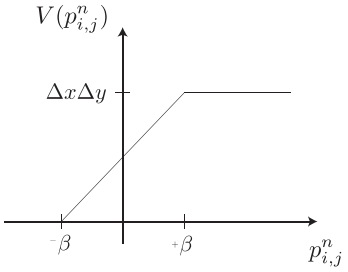

lengths occupied by the fluid and denoted by $\delta y_{i\pm\frac{1}{2}}$ and $\delta x_{ij\pm\frac{1}{2}}$, respectively, which are available to fluid flow through the edges.

2.3 | Semi-implicit discretization on a staggered grid

The domain is covered by the fluid and by the surrounding void via scalar volume fraction functions α, according to the so-called diffuse interface approach. Thus, the mass (volume) conservation equation in differential form reads

$$\partial_t \alpha + \partial_x(\alpha u) + \partial_y(\alpha v) = 0. \tag{6}$$

Integration of this mass conservation equation (6) over the space-time control volume $\Omega_{ij} = [x_{i-\frac{1}{2}}, x_{i+\frac{1}{2}}] \times [y_{j-\frac{1}{2}}, y_{j+\frac{1}{2}}] \times [t^n, t^{n+1}]$ and use of the Gauss theorem yield

$$\begin{aligned}\int_{x_{i-\frac{1}{2}}}^{x_{j+\frac{1}{2}}} \int_{y_{i-\frac{1}{2}}}^{y_{j+\frac{1}{2}}} \left(\alpha(x,y,t^{n+1}) - \alpha(x,y,t^n)\right)\, dydx + \int_{t^n}^{t^{n+1}} \int_{y_{j-\frac{1}{2}}}^{y_{j+\frac{1}{2}}} \left(\alpha u(x_{i+\frac{1}{2}},y,t) - \alpha u(x_{i-\frac{1}{2}},y,t)\right) dydt \\ + \int_{t^n}^{t^{n+1}} \int_{x_{i-\frac{1}{2}}}^{x_{i+\frac{1}{2}}} \left(\alpha v(x,y_{j+\frac{1}{2}},t) - \alpha v(x,y_{j-\frac{1}{2}},t)\right) dxdt = 0.\end{aligned} \tag{7}$$

With the definitions of the cell volume

$$V^n_{i,j} = \int_{x_{i-\frac{1}{2}}}^{x_{i+\frac{1}{2}}} \int_{y_{j-\frac{1}{2}}}^{y_{j+\frac{1}{2}}} \alpha(x,y,t) dydx, \tag{8}$$

and the fluxes

$$f_{i+\frac{1}{2},j} = \frac{1}{\Delta t \Delta y} \int_{t^n}^{t^{n+1}} \int_{y_{j-\frac{1}{2}}}^{y_{j+\frac{1}{2}}} \alpha u(x_{i+\frac{1}{2}},y,t) dydt, \qquad \text{and} \qquad g_{i,j+\frac{1}{2}} = \frac{1}{\Delta t \Delta x} \int_{t^n}^{t^{n+1}} \int_{x_{i-\frac{1}{2}}}^{x_{i+\frac{1}{2}}} \alpha v(x,y_{j+\frac{1}{2}},t) dxdt \tag{9}$$

the following integral form of (6) is obtained

$$V^{n+1}_{i,j} = V^n_{i,j} - \Delta t \Delta y (f_{i+\frac{1}{2},j} - f_{i-\frac{1}{2},j}) - \Delta t \Delta x (g_{ij+\frac{1}{2}} - g_{ij-\frac{1}{2}}). \tag{10}$$

Introducing the cell-average of the volume fraction

$$\alpha_{i,j}^{n} = \frac{1}{\Delta x \Delta y} \int_{x_{i-\frac{1}{2}}}^{x_{i+\frac{1}{2}}} \int_{y_{j-\frac{1}{2}}}^{y_{j+\frac{1}{2}}} \alpha(x,y,t) dy dx, \tag{11}$$

it is possible to rewrite (12) as

$$\alpha_{i,j}^{n+1} = \alpha_{i,j}^{n} - \frac{\Delta t}{\Delta x}(f_{i+\frac{1}{2},j} - f_{i-\frac{1}{2},j}) - \frac{\Delta t}{\Delta y}(g_{i,j+\frac{1}{2}} - g_{i,j-\frac{1}{2}}), \tag{12}$$

which is the integral form of (6). Assuming the velocity field constant along each edge and denoting these velocities at the new time by $u_{i+\frac{1}{2},j}^{n+1}$ and $v_{i,j+\frac{1}{2}}^{n+1}$, and defining the effective edge lengths that are occupied by the fluid as

$$\delta y_{i+\frac{1}{2},j}^{n+1} = \int_{y_{j-\frac{1}{2}}}^{y_{j+\frac{1}{2}}} \alpha(x_{i+\frac{1}{2}}, y, t^{n+1}) dy, \qquad \text{and} \qquad \delta x_{i,j+\frac{1}{2}}^{n+1} = \int_{x_{i-\frac{1}{2}}}^{x_{i+\frac{1}{2}}} \alpha(x, y_{j+\frac{1}{2}}, t^{n+1}) dx, \tag{13}$$

it is possible to define the following edge-averaged volume fractions

$$\alpha_{i+\frac{1}{2},j}^{n+1} = \frac{\delta y_{i+\frac{1}{2},j}^{n+1}}{\Delta y}, \qquad \text{and} \qquad \alpha_{i,j+\frac{1}{2}}^{n+1} = \frac{\delta x_{i,j+\frac{1}{2}}^{n+1}}{\Delta x}. \tag{14}$$

Defining the fluxes in terms of the edge velocities and the edge-averaged volume fractions as

$$f_{i+\frac{1}{2},j} = \alpha_{i+\frac{1}{2},j}^{n+1} \, u_{i+\frac{1}{2},j}^{n+1}, \qquad \text{and} \qquad g_{i,j+\frac{1}{2}} = \alpha_{i,j+\frac{1}{2}}^{n+1} \, v_{i,j+\frac{1}{2}}^{n+1} \tag{15}$$

the volume conservation equation (12) can finally be written as

$$V_{i,j}^{n+1} = V_{i,j}^{n} - \Delta t \left((\delta y u)_{i+\frac{1}{2},j}^{n+1} - (\delta y u)_{i-\frac{1}{2},j}^{n+1} \right) - \Delta t \left((\delta x v)_{i,j+\frac{1}{2}}^{n+1} - (\delta x v)_{i,j-\frac{1}{2}}^{n+1} \right). \tag{16}$$

Equation (16) represents an implicit finite volume discretization of the continuity equation, as the semi-implicit method proposed in Reference 1. For the two momentum equations in (1), a semi-implicit finite-difference discretization is derived in such a fashion that the pressure gradient is discretized implicitly. Additionally, the nonlinear advective and viscous terms in the momentum equation are discretized explicitly and represented by two nonlinear operators $(\delta y u)_{i+\frac{1}{2},j}^{*}$ and $(\delta x v)_{i,j+\frac{1}{2}}^{*}$. The semi-implicit discretization of the momentum equations reads

$$\begin{aligned} (\delta y u)_{i+\frac{1}{2},j}^{n+1} &= (\delta y u)_{i+\frac{1}{2},j}^{*} - \frac{\Delta t}{\Delta x} \delta y_{i+\frac{1}{2},j}^{n+1} \, (p_{i+1,j}^{n+1} - p_{i,j}^{n+1}), \\ (\delta x v)_{i,j+\frac{1}{2}}^{n+1} &= (\delta x v)_{i,j+\frac{1}{2}}^{*} - \frac{\Delta t}{\Delta y} \delta x_{i,j+\frac{1}{2}}^{n+1} \, (p_{i,j+1}^{n+1} - p_{i,j}^{n+1}). \end{aligned} \tag{17}$$

The explicit operators $(\delta y u)_{i+\frac{1}{2},j}^{*}$, $(\delta x v)_{i,j+\frac{1}{2}}^{*}$ for the discretization of the nonlinear convective terms are discretized in a conservative way and are given below. Note that these operators can be seen as an explicit discretization of the advection system of the flux-vector splitting scheme of Toro and Vázquez-Cendón.[37] For simplicity, neglecting the viscous terms, the advection subsystem of the flux-vector splitting scheme is represented by the following differential terms

$$\begin{aligned} &\partial_t(\alpha u) + \partial_x(u \alpha u) + \partial_y(v \alpha u) = 0, \\ &\partial_t(\alpha v) + \partial_x(u \alpha v) + \partial_y(v \alpha v) = 0. \end{aligned} \tag{18}$$

Once the edge-averaged volume fractions have been introduced, the transport of the two conserved quantities, $(\delta y u)_{i+\frac{1}{2},j}^{n}$ and $(\delta x v)_{i,j+\frac{1}{2}}^{n}$, is discretized in an explicit and conservative way as follows:

$$(\delta yu)^*_{i+\frac{1}{2},j} = (\delta yu)^n_{i+\frac{1}{2},j} - \frac{\Delta t}{\Delta x}\left(f^n_{i+1,j} - f^n_{i,j}\right) - \frac{\Delta t}{\Delta y}\left(g^n_{i+\frac{1}{2},j+\frac{1}{2}} - g^n_{i+\frac{1}{2},j-\frac{1}{2}}\right),$$
$$(\delta xv)^*_{i,j+\frac{1}{2}} = (\delta xv)^n_{i,j+\frac{1}{2}} - \frac{\Delta t}{\Delta x}\left(f^n_{i+\frac{1}{2},j+\frac{1}{2}} - f^n_{i-\frac{1}{2},j+\frac{1}{2}}\right) - \frac{\Delta t}{\Delta y}\left(g^n_{i,j+1} - g^n_{i,j}\right).$$

The numerical flux $f^n_{i,j}$, necessary to compute $(\delta yu)^*_{i+\frac{1}{2},j}$, is given by

$$f^n_{i,j} = \frac{1}{2}\left(u^n_{i+\frac{1}{2},j}(\delta yu)^n_{i+\frac{1}{2},j} + u^n_{i-\frac{1}{2},j}(\delta yu)^n_{i-\frac{1}{2},j}\right) - \frac{1}{2}|s^{max}|\left((\delta yu)^n_{i+\frac{1}{2},j} - (\delta yu)^n_{i-\frac{1}{2},j}\right), \tag{19}$$

which is similar to the *Rusanov flux*, see, for example, Reference 38, with the choice of the speed s^{max} equal to the maximum wave speed present on the right or left side, as $|s^{\max}| = \max(|2u^n_{i+\frac{1}{2},j}|, |2u^n_{i-\frac{1}{2},j}|)$. The numerical flux $g^n_{i+\frac{1}{2},j+\frac{1}{2}}$ in y-direction is given by

$$g^n_{i+\frac{1}{2},j+\frac{1}{2}} = \frac{1}{2}v_{i+\frac{1}{2},j+\frac{1}{2}}\left((\delta yu)^n_{i+\frac{1}{2},j+1} + (\delta yu)^n_{i+\frac{1}{2},j}\right) - \frac{1}{2}|v_{i+\frac{1}{2},j+\frac{1}{2}}|\left((\delta yu)^n_{i+\frac{1}{2},j+1} - (\delta yu)^n_{i+\frac{1}{2},j}\right), \tag{20}$$

where $v_{i+\frac{1}{2},j+\frac{1}{2}} = \frac{1}{2}(v^n_{i,j+\frac{1}{2}} + v^n_{i+1,j+\frac{1}{2}})$ is an average in x direction of $v^n_{i,j+\frac{1}{2}}$ and $v^n_{i+1,j+\frac{1}{2}}$ and in this case, the numerical flux, is reduced to an *upwind* method.

The terms related to liquid viscosity have been neglected up to this point. However, they can be easily considered by adding them to the explicitly discretized conservative quantities $(\delta yu)^*_{i+\frac{1}{2},j}$ and $(\delta xv)^*_{i,j+\frac{1}{2}}$. Denoting by $(\delta yu)^{*v}_{i+\frac{1}{2},j}$ the conservative quantity where the viscous terms are considered, it reads:

$$(\delta yu)^{*v}_{i+\frac{1}{2},j} = (\delta yu)^*_{i+\frac{1}{2},j} + \nu(\delta yu)^n_{i+\frac{1}{2},j}\left(\frac{\Delta t}{\Delta x}\left(\frac{u^n_{i+\frac{3}{2},j} - u^n_{i+\frac{1}{2},j}}{\Delta x} - \frac{u^n_{i+\frac{1}{2},j} - u^n_{i-\frac{1}{2},j}}{\Delta x}\right) + \frac{\Delta t}{\Delta y}\left(\frac{u^n_{i,j+\frac{3}{2}} - u^n_{i,j+\frac{1}{2}}}{\Delta y} - \frac{u^n_{i,j+\frac{1}{2}} - u^n_{i,j-\frac{1}{2}}}{\Delta y}\right)\right). \tag{21}$$

The approach used for the operator in x direction $(\delta yu)^{*v}_{i+\frac{1}{2},j}$ can be easily applied to obtain the expression for the second explicit transport operator $(\delta xv)^{*v}_{i,j+\frac{1}{2}}$, necessary for the discrete momentum equation in y direction. Higher order in space and time can be achieved at the aid of a MUSCL-Hancock TVD method, see Reference 38 for details.

Inserting the discrete momentum equations (17) into the finite volume discretization of the continuity equation (16) yields the following preliminary system for the unknown pressure $p^{n+1}_{i,j}$

$$V(p^{n+1}_{i,j}) - \frac{\Delta t^2}{\Delta x}\left(\delta y^{n+1}_{i+\frac{1}{2},j}(p^{n+1}_{i+1,j} - p^{n+1}_{i,j}) - \delta y^{n+1}_{i-\frac{1}{2},j}(p^{n+1}_{i,j} - p^{n+1}_{i-1,j})\right)$$
$$- \frac{\Delta t^2}{\Delta y}\left(\delta x^{n+1}_{i,j+\frac{1}{2}}(p^{n+1}_{i,j+1} - p^{n+1}_{i,j}) - \delta x^{n+1}_{i,j-\frac{1}{2}}(p^{n+1}_{i,j} - p^{n+1}_{i,j-1})\right) = b^n_{i,j}, \tag{22}$$

with the known right-hand side $b^n_{i,j}$

$$b^n_{i,j} = V(p^n_{i,j}) - \Delta t\left((\delta yu)^{*v}_{i+\frac{1}{2},j} - (\delta yu)^{*v}_{i-\frac{1}{2},j}\right) - \Delta t\left((\delta xv)^{*v}_{i,j+\frac{1}{2}} - (\delta xv)^{*v}_{i,j-\frac{1}{2}}\right). \tag{23}$$

Discretizing also the edge-averaged volume fractions $\delta x^{n+1}_{i,j+\frac{1}{2}}$ implicitly, the system (22) becomes strongly nonlinear and thus difficult to solve. Therefore, a *Picard iteration* technique has to be adopted in order to make $\delta x^{n+1}_{i,j+\frac{1}{2}}$ again explicit, as suggested in Reference 39. Introducing k to denote the index of the Picard iterations, the following *piecewise linear* system for the pressure $p^{n+1,k+1}_{i,j}$ is obtained

$$V(p^{n+1,k+1}_{i,j}) - \frac{\Delta t^2}{\Delta x}\left(\delta y^{n+1,k}_{i+\frac{1}{2},j}(p^{n+1,k+1}_{i+1,j} - p^{n+1,k+1}_{i,j}) - \delta y^{n+1,k}_{i-\frac{1}{2},j}(p^{n+1,k+1}_{i,j} - p^{n+1,k+1}_{i-1,j})\right)$$
$$- \frac{\Delta t^2}{\Delta y}\left(\delta x^{n+1,k}_{i,j+\frac{1}{2}}(p^{n+1,k+1}_{i,j+1} - p^{n+1,k+1}_{i,j}) - \delta x^{n+1,k}_{i,j-\frac{1}{2}}(p^{n+1,k+1}_{i,j} - p^{n+1,k+1}_{i,j-1})\right) = b^n_{i,j}. \tag{24}$$

The quantities $\delta y^{n+1,k}_{i+\frac{1}{2},j}$ and $\delta x^{n+1,k}_{i,j+\frac{1}{2}}$ are defined as

$$\delta y^{n+1,k}_{i+\frac{1}{2},j} = \Delta y \frac{1}{2}\left(\alpha(p^{n+1,k}_{i,j}) + \alpha(p^{n+1,k}_{i+1,j})\right) = \frac{1}{2\Delta x}\left(V(p^{n+1,k}_{i,j}) + V(p^{n+1,k}_{i+1,j})\right), \tag{25}$$

$$\delta x^{n+1,k}_{i,j+\frac{1}{2}} = \Delta x \frac{1}{2}\left(\alpha(p^{n+1,k}_{i,j}) + \alpha(p^{n+1,k}_{i,j+1})\right) = \frac{1}{2\Delta y}\left(V(p^{n+1,k}_{i,j}) + V(p^{n+1,k}_{i,j+1})\right). \tag{26}$$

The system (24) needs to be solved for the pressure $p^{n+1,k+1}_{i,j}$ at each Picard iteration. Using a more compact notation, the above system can be written as follows

$$\boldsymbol{V}(\boldsymbol{p}^{n+1,k+1}) + \boldsymbol{T}\boldsymbol{p}^{n+1,k+1} = \boldsymbol{b}^{n}, \tag{27}$$

with the vector of the unknown new pressure $\boldsymbol{p}^{n+1,k+1} = (p^{n+1,k+1}_{i,j})$ and where $\boldsymbol{V}(\boldsymbol{p^{n+1,k+1}}) = \left(V(p^{n+1,k+1}_{i,j})\right)$ denotes the corresponding fluid volumes; $\boldsymbol{b}^{n}$ is the known right-hand side vector and $\boldsymbol{T}$ is a sparse, symmetric, and penta-diagonal matrix which arises from the linear terms in Equation (24). The matrix $\boldsymbol{T}$ in the system (27) is symmetric and at least positive semi-definite. For the solution of system (27), we apply the nested Newton-type technique introduced by Casulli et al.,[28,29,39,40] associated with a matrix-free implementation of the conjugate gradient method. For implementation details and the convergence proofs of these Newton-type techniques applied to mildly nonlinear systems, the reader is referred to the above references.

Once the pressures $p^{n+1,k+1}_{i,j}$ are evaluated, the quantities $\delta y^{n+1,k}_{i+\frac{1}{2},j}$ and $\delta x^{n+1,k}_{i,j+\frac{1}{2}}$ at the next Picard iteration can be easily obtained from (25) and (26). As confirmed by numerical simulations, only very few Picard iterations are needed to obtain an accurate solution. In all test problems shown in this article, three Picard iterations are assumed.

At the end of the last Picard iteration $p^{n+1}_{i,j} := p^{n+1,k+1}_{i,j}$ is set and the velocity field is easily obtained from the discrete momentum equations (17) as follows:

$$\begin{aligned}(\delta yu)^{n+1}_{i+\frac{1}{2},j} &= (\delta yu)^{*}_{i+\frac{1}{2},j} - \frac{\Delta t}{\Delta x}\delta y^{n+1}_{i+\frac{1}{2},j}(p^{n+1}_{i+1,j} - p^{n+1}_{i,j}),\\ (\delta xv)^{n+1}_{i,j+\frac{1}{2}} &= (\delta xv)^{*}_{i,j+\frac{1}{2}} - \frac{\Delta t}{\Delta y}\delta x^{n+1}_{i,j+\frac{1}{2}}(p^{n+1}_{i,j+1} - p^{n+1}_{i,j}).\end{aligned} \tag{28}$$

The resulting scheme is written in flux form for both conservation equations, hence is formulated to be locally and globally conservative for both mass and momentum. For this reason, it is also suitable for dealing with shock waves and dambreak problems. The stability condition, followed by the time step is only limited by a *mild* CFL condition based on the flow speed. The stability condition, followed by the time step is only limited by a *mild* CFL condition based on the flow speed. It can be shown, see Casulli and Cattani,[41] that the numerical stability of the semi-implicit method, represented by (16) and (17), depends only on the choice of the operators f and g used for the discretization of the nonlinear convective terms $(\delta yu)^{n}_{i+\frac{1}{2},j}$ and $(\delta xv)^{n}_{i,j+\frac{1}{2}}$. In (19) and (20), a *Rusanov type flux* is proposed and then CFL time restriction reads:

$$\Delta t \leq \frac{1}{\frac{s^{max}_{u}}{\Delta x} + \frac{2\nu}{\Delta x^2} + \frac{s^{max}_{v}}{\Delta y} + \frac{2\nu}{\Delta y^2}}. \tag{29}$$

Therefore, the stability condition is not affected by the gravity wave speed, thus rendering the method efficient for *low Froude number* flows, too. The proposed method has been presented in its simplest form. It represents a rather general framework for future developments of more accurate and complete models, in terms of multi-physics problems in general and incompressible and weakly compressible multi-phase flows in particular.

An extension of the semi-implicit part to up to second order in time can be achieved at the aid of the so-called θ-method, where $\theta = 0.5$ reduces to the Crank–Nicolson method. In this case, the discrete momentum and continuity equations become:

$$\begin{aligned}(\delta yu)^{n+1}_{i+\frac{1}{2},j} &= (\delta yu)^{*}_{i+\frac{1}{2},j} - \frac{\Delta t}{\Delta x}\delta y^{n}_{i+\frac{1}{2},j}(p^{n+\theta}_{i+1,j} - p^{n+\theta}_{i,j}),\\ (\delta xv)^{n+1}_{i,j+\frac{1}{2}} &= (\delta xv)^{*}_{i,j+\frac{1}{2}} - \frac{\Delta t}{\Delta y}\delta x^{n}_{i,j+\frac{1}{2}}(p^{n+\theta}_{i,j+1} - p^{n+\theta}_{i,j}),\end{aligned} \tag{30}$$

and

$$V_{i,j}^{n+1} = V_{i,j}^{n} - \Delta t \left((\delta yu)_{i+\frac{1}{2},j}^{n+\theta} - (\delta yu)_{i-\frac{1}{2},j}^{n+\theta} \right) - \Delta t \left((\delta xv)_{i,j+\frac{1}{2}}^{n+\theta} - (\delta xv)_{i,j-\frac{1}{2}}^{n+\theta} \right) \tag{31}$$

with the pressure and the momentum at the intermediate time level given by

$$p_{i,j}^{n+\theta} = (1-\theta)\, p_{i,j}^{n} + \theta p_{i,j}^{n+1}, \tag{32}$$

$$(\delta yu)_{i+\frac{1}{2},j}^{n+\theta} = (1-\theta)\, (\delta yu)_{i+\frac{1}{2},j}^{n} + \theta (\delta yu)_{i+\frac{1}{2},j}^{n+1}, \quad (\delta xv)_{i,j-\frac{1}{2}}^{n+\theta} = (1-\theta)(\delta xv)_{i,j-\frac{1}{2}}^{n} + \theta (\delta xv)_{i,j-\frac{1}{2}}^{n+1}. \tag{33}$$

The resulting pressure system then reads

$$\begin{aligned} V(p_{i,j}^{n+1}) &- \theta^2 \frac{\Delta t^2}{\Delta x} \left(\delta y_{i+\frac{1}{2},j}^{n} (p_{i+1,j}^{n+1} - p_{i,j}^{n+1}) - \delta y_{i-\frac{1}{2},j}^{n} (p_{i,j}^{n+1} - p_{i-1,j}^{n+1}) \right) \\ &- \theta^2 \frac{\Delta t^2}{\Delta y} \left(\delta x_{i,j+\frac{1}{2}}^{n} (p_{i,j+1}^{n+1} - p_{i,j}^{n+1}) - \delta x_{i,j-\frac{1}{2}}^{n} (p_{i,j}^{n+1} - p_{i,j-1}^{n+1}) \right) = b_{i,j}^{n} \end{aligned} \tag{34}$$

with the right-hand side

$$\begin{aligned} b_{i,j}^{n} = V(p_{i,j}^{n}) &- \theta \Delta t \left((\delta yu)_{i+\frac{1}{2},j}^{*} - (\delta yu)_{i-\frac{1}{2},j}^{*} \right) - \theta \Delta t \left((\delta xv)_{i,j+\frac{1}{2}}^{*} - (\delta xv)_{i,j-\frac{1}{2}}^{*} \right) \\ &- (1-\theta) \Delta t \left((\delta yu)_{i+\frac{1}{2},j}^{n} - (\delta yu)_{i-\frac{1}{2},j}^{n} \right) - (1-\theta) \Delta t \left((\delta xv)_{i,j+\frac{1}{2}}^{n} - (\delta xv)_{i,j-\frac{1}{2}}^{n} \right) \\ &- \theta(1-\theta) \frac{\Delta t^2}{\Delta x} \left(\delta y_{i+\frac{1}{2},j}^{n} (p_{i+1,j}^{n} - p_{i,j}^{n}) - \delta y_{i-\frac{1}{2},j}^{n} (p_{i,j}^{n} - p_{i-1,j}^{n}) \right) \\ &- \theta(1-\theta) \frac{\Delta t^2}{\Delta y} \left(\delta x_{i,j+\frac{1}{2}}^{n} (p_{i,j+1}^{n} - p_{i,j}^{n}) - \delta x_{i,j-\frac{1}{2}}^{n} (p_{i,j}^{n} - p_{i,j-1}^{n}) \right). \end{aligned} \tag{35}$$

2.4 | Remark

When the vertical mesh spacing Δy is large enough to contain the entire water layer of depth H, we can drop the vertical index j and set $(\delta y)_{i+1/2}^{n} = H_{i+1/2}^{n}$. Since for one single layer $p_i^n = g(\eta_i^n - y_b)$ with η_i^n the free surface elevation and y_b the location of the barycenters of the only row of cells in y direction, the previous scheme reduces to

$$V_i^{n+1} = V_i^n - \Delta t \left((Hu)_{i+\frac{1}{2}}^{n+1} - (Hu)_{i-\frac{1}{2}}^{n+1} \right), \tag{36}$$

$$(Hu)_{i+\frac{1}{2}}^{n+1} = (Hu)_{i+\frac{1}{2}}^{*} - \frac{\Delta t}{\Delta x} H_{i+\frac{1}{2}}^{n} (p_{i+1}^{n+1} - p_i^{n+1}), \tag{37}$$

which is a consistent and mass and momentum conservative discretization of the 1D shallow water equations

$$\frac{\partial \eta}{\partial t} + \frac{\partial (Hu)}{\partial x} = 0, \tag{38}$$

$$\frac{\partial (Hu)}{\partial t} + \frac{\partial (Hu^2)}{\partial x} + gH \frac{\partial \eta}{\partial x} = 0. \tag{39}$$

3 | NUMERICAL RESULTS

In the following, we present some numerical results obtained with the new scheme proposed in this article. For validation purposes, we first run the method with only one vertical layer, where the scheme automatically reduces to a

consistent mass and momentum conservative method for the 1D shallow water equations according to (36) and (37). This is achieved by taking the vertical resolution Δy at least as large as the maximum vertical height of the flow. In particular, the method is used to solve some 1D Riemann problems, for which the exact solution is known, see Reference 42. After this validation in the shallow water limit, some computational results for non-hydrostatic problems with single and multi-valued free surface are shown, as well as a very simple flow around a rigid solid obstacle. In all the tests, the global mass and momentum conservation have been checked and were found to be conserved for all times.

3.1 | Dambreak problems

The so-called dambreak problem is a common test for numerical methods applied to the shallow-water equations. It consists of removing a vertical weir instantly, which separates two different piecewise constant states of water from each other. In the initial stages of dambreak flow, the shallow water assumption of small vertical velocities and accelerations does not hold. For this reason, it is of interest to apply a more complete model that is able to deal with non-hydrostatic flows. First, in this section the new numerical method proposed in this article is run on a mesh that consists of only vertical layer and thus simplifies to a consistent and conservative discretization of the hydrostatic one-dimensional shallow water equations. The obtained results are compared against the exact solutions of the shallow water equations, both, for the wet bed and for the dry bed case. For exact solutions of the Riemann problem of the shallow water equations see Reference 42.

Then, in 2D, it is interesting to compare the behavior at small times and at large times with each other. For an experimental study of the initial instants of dambreak flow, see, for example, Reference 43.

3.1.1 | Hydrostatic simulations with only one vertical layer

The two-dimensional conservative method is simplified to a discretization of the hydrostatic one-dimensional equations by taking the vertical resolution Δy as large as the maximum vertical flow height. This one-dimensional resulting method is used to solve the following 1D Riemann problems, which represent the dambreak problem over a wet bed and over a dry one. The exact solution of the dambreak problem over a dry bed has been derived by Ritter.[44] The tests are run over a fixed spatial domain $\Omega = [-0.5; 0.5] \times [0; 1]$ covered by a uniform grid consisting of 100×1 cells, with mesh spacing $\Delta x = 0.01$ in the x-direction, while in the vertical y-axis, oriented upward along the gravity direction, a single cell of size $\Delta y = 1$ is taken. The simulations are carried out using a CFL number of CFL $= 0.9$, based on the maximum eigenvalue of the system, until the final time. For the first Riemann problem, RP1, the initial left and right states are defined as follows: $\eta_L = 1$, $\eta_R = 0.1$ for the initial free surface elevation of the water and $u_L = u_R = 0$ for the velocities. The pressures are in an initially hydrostatic condition and are computed from η. This situation represents the dam break over a wet bed. For the second Riemann problem, RP2, the initial left and right states are defined as follows: $\eta_L = 1$, $\eta_R = 0$ for the initial free surface elevation of the water and $u_L = u_R = 0$ for the velocities. This configuration represents the dam break over a dry bed. Wall friction and fluid viscosity are neglected, and the gravity is assumed to be constant and equal to $g = 1$. The results obtained with the new method are depicted for RP1 in Figure 3 and for RP2 in Figure 4. These figures clearly show that the problems are solved correctly even in the numerically more complex case over a dry bed. In Figure 3, it is possible to observe that the shock is located in the right position and the post-shock values are also correct. It is furthermore possible to note the typical numerical dissipation (numerical viscosity) at the waves, which, however, is reasonably low for the numerical method used here, since the shock wave is well resolved. In Figure 4, the Riemann problem over a dry bed is shown and compared against the exact solution of the shallow water equations obtained by Ritter.[44] In this case, there are no shock waves involved and the flow can be considered as smooth. An important task is the verification of the expected accuracy of a numerical method, which in this case has to be first-order accurate due to the presence of discontinuities in the solution. To verify this order of accuracy, various numerical solutions of RP1 with different mesh sizes are considered. Since the exact value for h or for hu is known, the standard way to get a precise number for the order of accuracy is to halve the mesh spacing and to look at the ratio of the errors. Denoting by Δx_k the mesh spacing of mesh k considered in the study, the numerical convergence rate O_{L^1} can be computed as

$$\log\left(\frac{L^1_{k-1}}{L^1_k}\right) / \log\left(\frac{\Delta x_{k-1}}{\Delta x_k}\right) = \mathcal{O}(L^1_k), \tag{40}$$

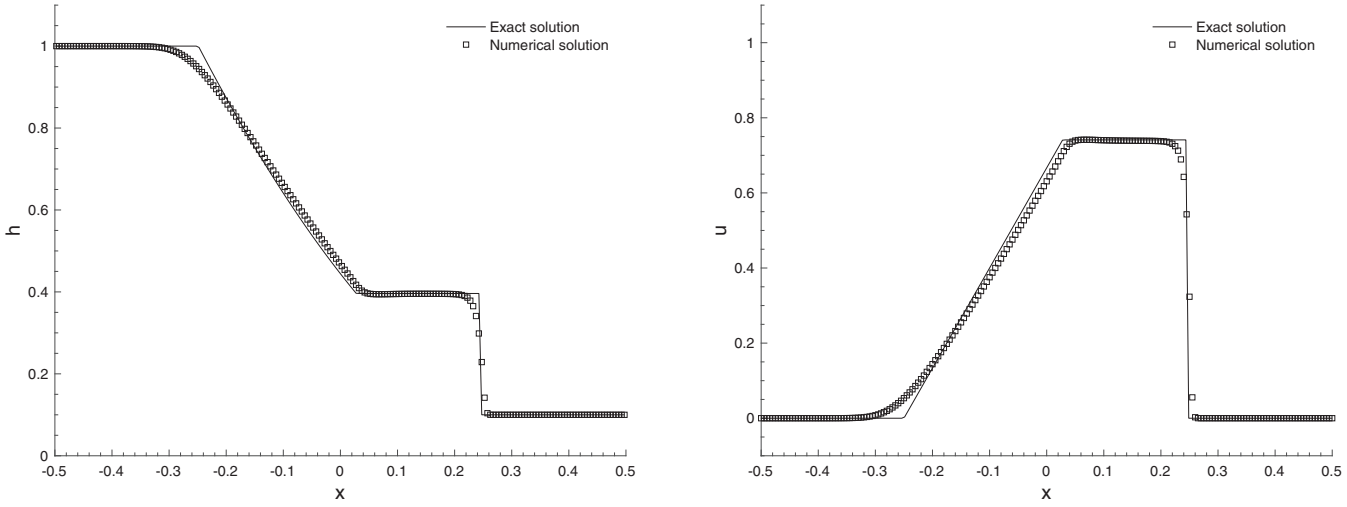

FIGURE 3 Exact and numerical solutions evaluated with the conservative method for the (RP1), at time 0.25 s

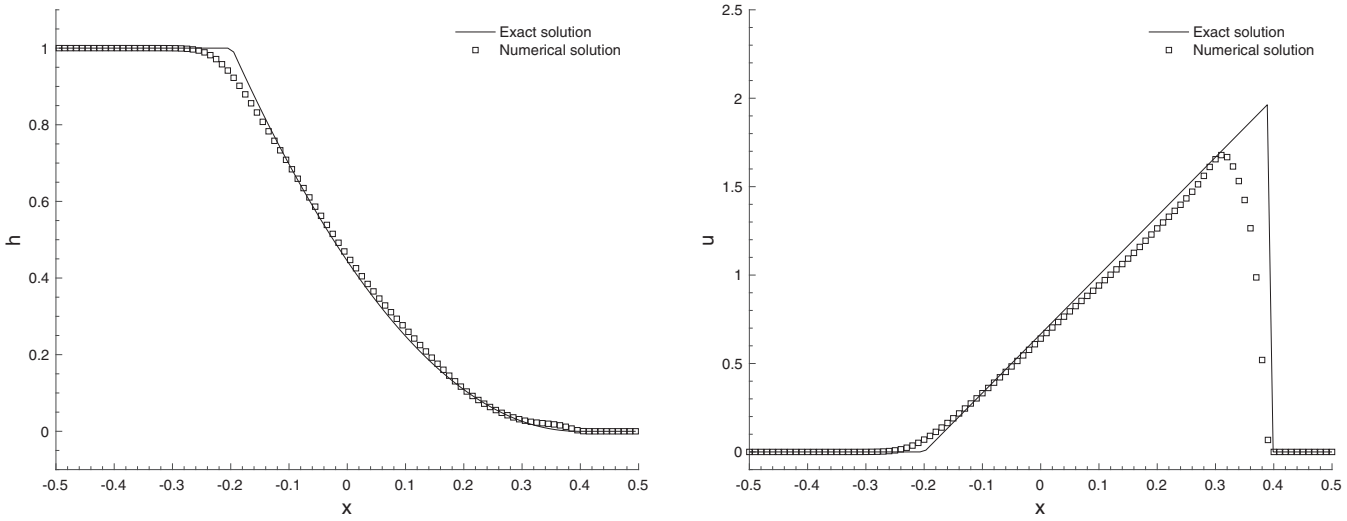

FIGURE 4 Exact and numerical solutions evaluated with the conservative method for the (RP2), at time 0.2 s

where L_k^1 is the L^1 error on mesh k. The second column of Table 1 shows the mesh size Δx_k for the sequence of meshes; in the third column the number of elements N_d are reported; the fourth column shows the errors norms L_k^1; and the last column contains the corresponding convergence rates $\mathcal{O}(L^1)$. As expected, for this discontinuous problem, our mass and momentum conservative scheme converges to the exact solution of the Riemann problem with first order of accuracy. In Figure 5, the L^1 error is represented graphically against the number of elements of the mesh. For the new conservative method, the empirically obtained convergence rates are consistent with the theoretically expected first order of accuracy. Furthermore, in the same figure it is also possible to see that when the convective terms are discretized with a second order MUSCL-Hancock scheme in time and space in combination with the θ-method to approximate the remaining system, globally, the method remains first order accurate due to discontinuities in the solution, as expected. However, for the same mesh, the solution is more accurate using the θ method in combination with the MUSCL-Hancock scheme.

3.1.2 | Non-hydrostatic simulations with multiple vertical layers

In this case, the governing equations solved for the following numerical examples are the incompressible Euler equations without any simplification concerning the number of layers in y-direction. To achieve this, it is enough to take multiple

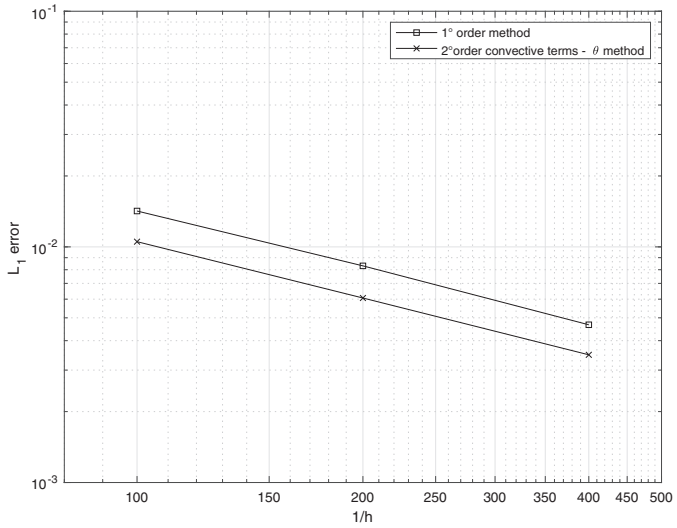

FIGURE 5 Error against the number of elements of the mesh, for both the simplest conservative method and one modified to improve accuracy

k	Δx_k	N_d	L^1	O_{L^1}
1	0.01	100	1.420E-02	
2	0.005	200	8.307E-03	0.77
3	0.0025	400	4.671E-03	0.93

TABLE 1 Numerical convergence rates for the conservative method

vertical layers, which means taking the vertical resolution Δy smaller than the maximum vertical flow height. In this manner, the non-hydrostatic behavior of the flow is preserved.

Dry bed

First, the classical dambreak over a dry bed is presented. As mentioned before, the exact solution to this problem, using the hydrostatic shallow-water model, is the Ritter solution. The rectangular computational domain is $\Omega = [-5; 5] \times [0; 2]$, the fluid is at rest and is confined in the leftmost part of the domain $\Omega_l = [-5; 0] \times [0; 1.5]$. The velocities are imposed equal to zero $u = v = 0$ everywhere and the pressure is set in order to get an initially hydrostatic pressure profile $p^0_{i,j} = g(\eta(x_i, 0) - y_j)$. The domain is covered by a uniform grid consisting of 200,000 cells, with mesh spacing $\Delta x = 0.01$, $\Delta y = 0.01$ in both the x-direction and y-direction. The simulations are carried out using a Courant–Friedrichs–Lewy number of CFL $= 0.9$, based on the maximum eigenvalue of the system until the final time $t_{end} = 0.5$. The boundary conditions are reflective wall on all the borders of the computational domain Ω. Wall friction and fluid viscosity are neglected, and the gravity is assumed to be constant and equal to $g = 9.81$. The results obtained at time $t = 0.5$ with our new method proposed in this article are presented in Figure 6. The results are compared against the exact solution of the shallow water equations obtained by Ritter[44] for each time. At early times, the non-hydrostatic results are in good agreement with the previously computed results by Dumbser,[30] which have been compared with the results obtained by the smooth particle hydrodynamics (SPH) scheme of Ferrari et al..[45] It can be shown that the free-surface profile tends to be a good approximation of the analytical solution of the one-dimensional shallow water equations only as the spatial and the temporal domain increase. This is in total agreement with the fact that in the initial times, the vertical acceleration, as well as the pressure gradient in the vertical direction, are the main component of the flow, and thus the hydrostatic pressure assumption of the shallow water model is not verified. This initially strongly non-hydrostatic behavior can also be seen in the pressure field depicted in Figure 6. Here, the pressure field turns sharply to the x-axis until it becomes orthogonal to it.

Wet bed

Here, a dambreak into a wet bed case is considered. The rectangular computational domain is $\Omega = [-7.5; 5] \times [0; 2]$. The fluid is initially at rest and is confined in both the left and right parts of the domain, that is, the initial liquid domain is $\Omega_l = ([-7.5; 0] \times [0; 1.5]) \cup ([0; 5] \times [0; 0.75])$. The velocities are imposed equal to zero $u = v = 0$ everywhere and the pressure is set in order to get two different initial hydrostatic pressure profiles $p^0_{i,j} = g(\eta(x_i, 0) - y_j)$. The domain is covered by a uniform grid consisting of 250,000 cells, with mesh spacing $\Delta x = 0.01$ in the x-direction, $\Delta y = 0.01$ in the y-direction.

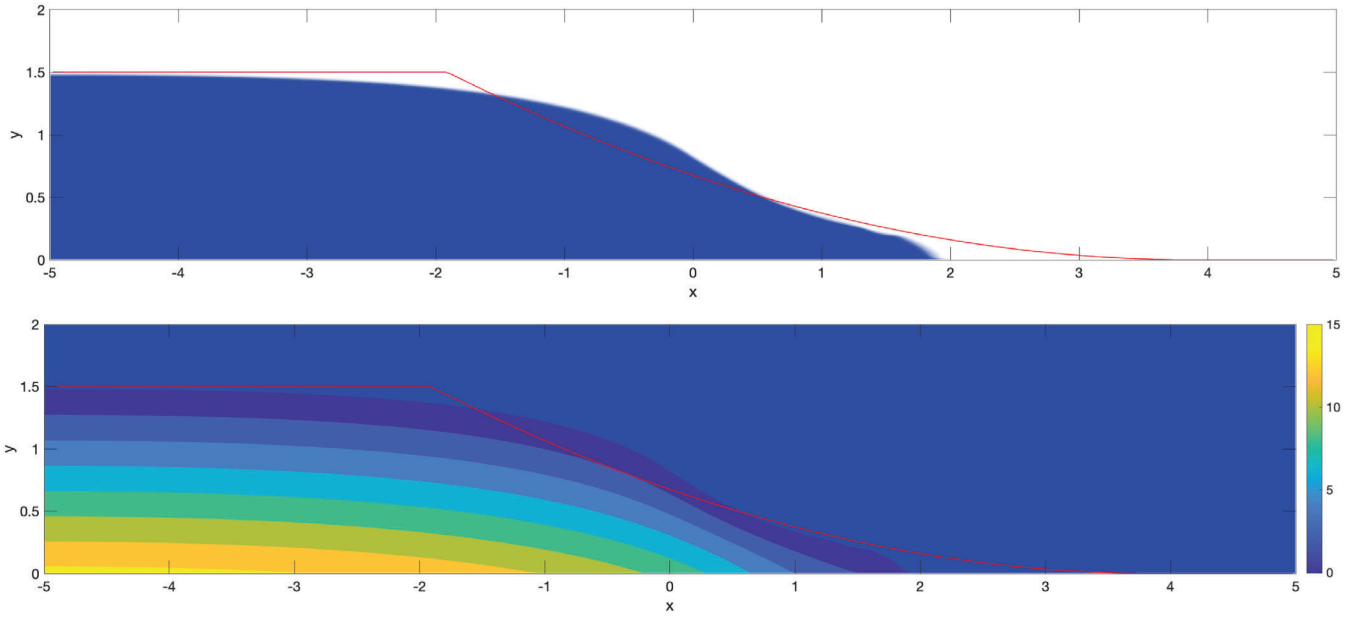

FIGURE 6 Numerical solutions for free surface profile and pressure field, evaluated with the 2D non-hydrostatic conservative methods for the dambreak into dry bed problem, at time $t = 0.5$. In the first row, the volume fraction (density contours) and shallow water model (red line) are represented. In the second row, pressure field is depicted [Colour figure can be viewed at wileyonlinelibrary.com]

The CFL, and the boundary conditions are the same as for the dambreak into dry bed. Wall friction and fluid viscosity are neglected, and the gravity is assumed to be constant and equal to $g = 9.81$. The computation is carried out until the final time $t_{end} = 1$. Experimental observations[46] show that wave breaking can occur in a dambreak into a wet bed. However, the higher the water level on the right side of the dam, the smaller becomes the breaking wave. In this test case, the level of the right layer of water is quite high, so at most, a very small breaking wave can occur. At the time $t = 1.0$, in Figure 7, small-scale free surface waves are visible in the constant region between the shock and the rarefaction wave. Again, the results are in agreement with those previously obtained by the two-phase flow model of Dumbser[30] and by the SPH method of Ferrari et al..[45-47] Furthermore, the solution is even closer to the one achieved with the SPH method. In fact, smaller surface waves are predicted by the latter and particularly it shows a small breaking of waves at the moving right front. In Figure 7, the volume fraction shows a tendency for the crest of the wave to break via smaller volume fractions. We emphasize that at the initial stages the obtained solution does not agree with the solution of the shallow-water model, represented by a red line in Figure 7. This disagreement, for short times, is due to the fact that the hydrostatic shallow water model neglects vertical accelerations, which are quite important in the early stages of dambreak flow.

Wet bed with bottom step

The last dambreak problem is into a wet bed with a bottom step. This problem is similar to the previous one. The only difference is that a step of height $h_s = 0.2$ is introduced in the bottom from $x = 0$ to $x = 5$. As described in Section 2.3, the domain is covered by the fluid and by the surrounding void via scalar volume fraction functions, according to the so-called diffuse interface approach. For this reason, it is obvious to treat also fixed and kinematically moving rigid obstacles contained in the computational domain, via two different scalar volume fraction functions for water α_w and solid bodies α_s. Therefore, the step in the domain is treated as a solid obstacle where there cannot be any liquid volume fraction. The computational domain is $\Omega = [-7.5; 5] \times [0; 2]$ and the initial domain covered by the liquid is $\Omega_l = ([-7.5; 0] \times [0; 1.5]) \cup ([0; 5] \times [0.2; 0.5])$. The velocities are imposed equal to zero $u = v = 0$ everywhere and pressure is set in order to get two different initial hydrostatic pressure profiles $p^0_{i,j} = g(\eta(x_i, 0) - y_j)$. The mesh, the CFL number and the boundary conditions are the same as for the other dambreak problems. Wall friction and fluid viscosity are neglected, and the gravity is assumed to be constant and equal to $g = 9.81$. The computation is carried out until the final time $t_{end} = 1$. The computational results are depicted at time $t = 1.0$ in Figure 8. The obtained results agree qualitatively with those obtained in References 30 and 45. However, it is interesting to see how model is accurate evaluating the pressure field and

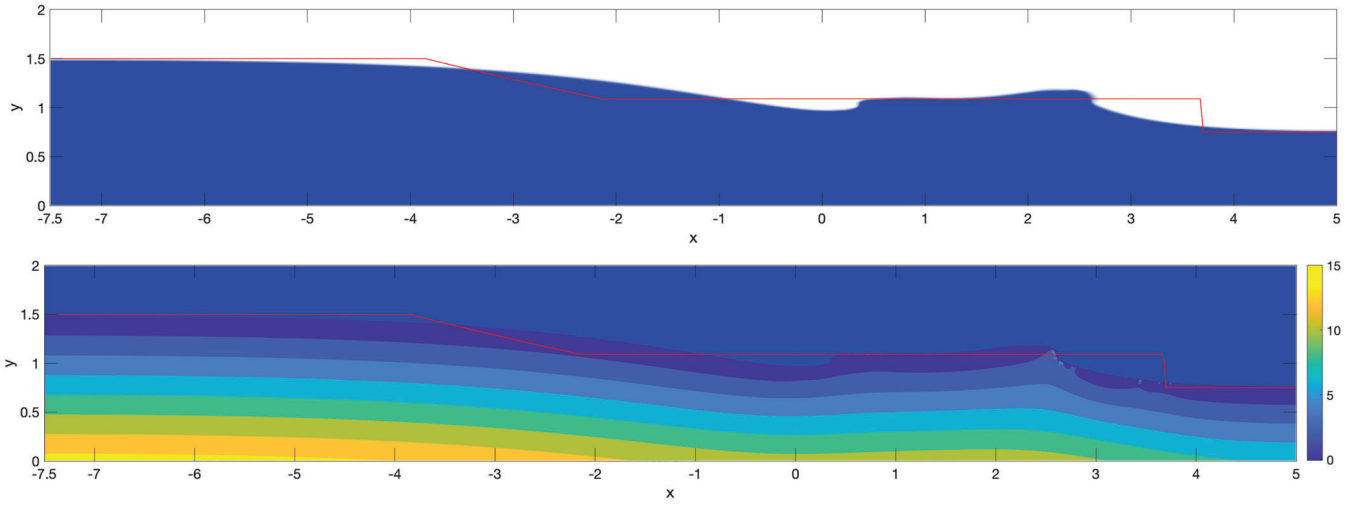

FIGURE 7 Numerical solutions for free surface profile and pressure field, evaluated with the 2D non-hydrostatic conservative methods for the dambreak into wet bed problem, at time $t = 1.0$. In the first row, the volume fraction (density contours) and shallow water model (red line) are represented. In the second row, pressure field is depicted [Colour figure can be viewed at wileyonlinelibrary.com]

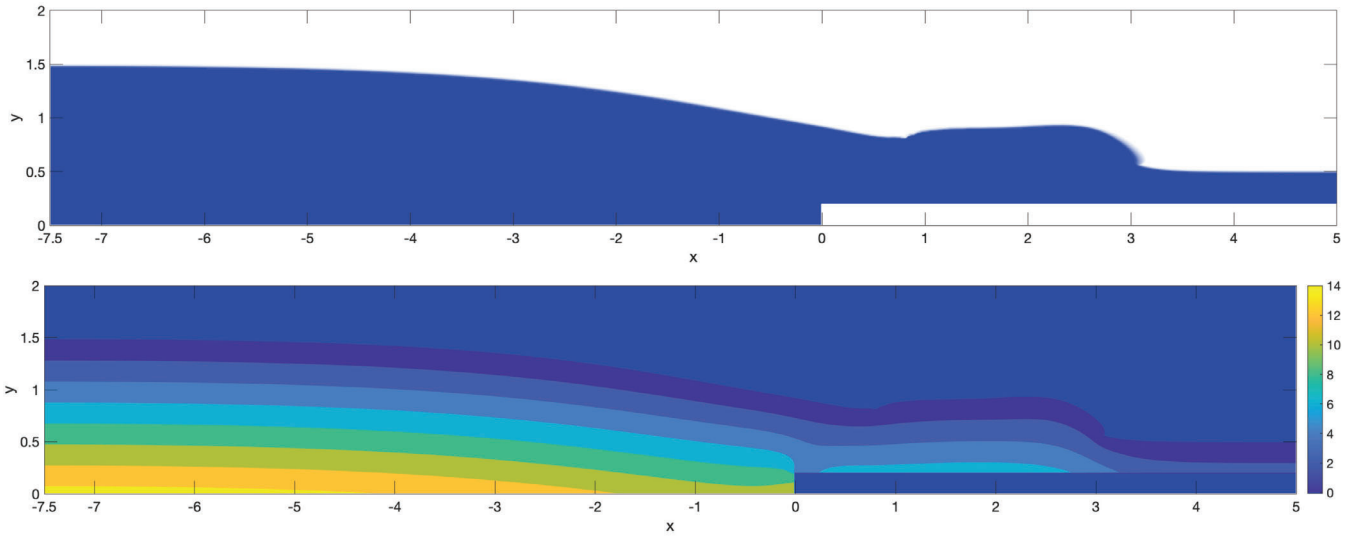

FIGURE 8 Numerical solutions for free surface profile and pressure field, evaluated with the 2D non-hydrostatic conservative methods for the dambreak over a bottom step into wet bed at time wet bed, at time $t = 1.0$. In the first row, the volume fraction (density contours) is represented. In the second row, pressure field is depicted [Colour figure can be viewed at wileyonlinelibrary.com]

the recirculation zone in the vicinity of the bottom step, in Figure 9. Furthermore, this example also shows the ability of the method to treat well rigid obstacles contained in the computational domain.

3.2 | Flow over a weir

In this section, the flow over a sharp-crested weir is presented. The rectangular computational domain is $\Omega = [0; 12] \times [0; 2]$. It contains an infinitely thin, sharp weir of height $h = 1.2$, which is located at $x = 7.5$ and is modeled as a reflective wall boundary. The fluid is initially at rest and is confined in the leftmost part of the domain $\Omega_l = [0; 7.5] \times [0; 2]$, which leads to a level of water over the weir. Velocities are imposed equal to zero $u = v = 0$ everywhere and the pressure is set in order to get an initially hydrostatic pressure profile. Wall friction and fluid viscosity are neglected, and the

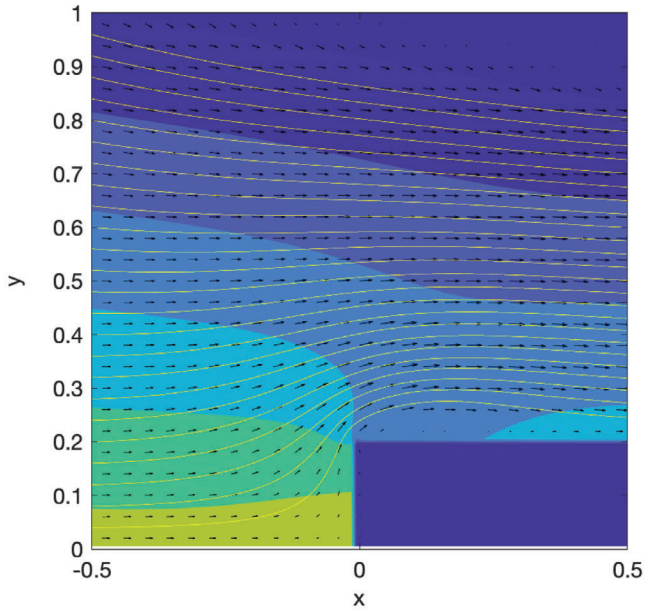

FIGURE 9 Zoom into the recirculation zone in the vicinity of the bottom step for the pressure field, at time $t = 1.0$. The velocity field and the streamline (yellow solid line) are also shown [Colour figure can be viewed at wileyonlinelibrary.com]

gravity is assumed to be constant and equal to $g = 9.81$. The domain is covered by a uniform grid consisting of 240,000 cells, with mesh spacing $\Delta x = 0.01$ in the x-direction and $\Delta y = 0.01$ in the y-direction. The computation is carried out using a Courant–Friedrichs–Lewy number of CFL = 0.9 until the final time $t_{end} = 1$. The boundary conditions are reflective wall on all the borders of the computational domain Ω. For times close to t = 1.0, the overflow profile is rather steady and it is possible to compare it with the experimental reference solution of the profile found by Scimemi.[48] The lower streamline of this experimental reference solution can be evaluated, as reported in Reference 49, by the following equation:

$$y(x) = y_m - 0.47 h_o \left(\frac{x - x_m}{h_o} \right)^{1.85}, \tag{41}$$

where x_m and y_m are the coordinates of the maximum of the curve, and h_o is the vertical distance between the crest of the weir and the free surface at the weir's location. The computational results obtained at the time $t = 1.0$ are depicted in Figure 10, and a zoom of the overflow profile is shown in Figure 11. According to the obtained results, it is possible to evaluate the quantities required to assess the experimental reference solution of Scimeni (41). These quantities are $x_m = 7.636$, $y_m = 1.236$, and $h_o = 0.4040$, see also Reference 49. In Figures 10 and 11, the reference solution, evaluated by these quantities, is shown as a red solid line. It can be seen that the numerical results are in good agreement with the experimental reference solution.

In this test, some of the most relevant features of this novel momentum-conservative scheme can be seen. First, the ability to model non-hydrostatic free surface flows with a multi-valued free surface is evident. In addition, the flow results from the interaction of a liquid with a fixed rigid obstacle contained in the computational domain. These features arise from the so-called diffuse interface approach, which has been adopted to describe the domain. The domain is covered by the fluid and by the solid via two different scalar volume fraction functions for water and solid bodies. Moreover, the so-called diffuse interface approach provides a solution that is suitable for situations in which changes of the interface topology are involved (e.g., breaking a water jet into drops as in flow over a weir). Therefore, as it is shown in Figure 11, the model also allows to evaluate what is a break in drops of the overflow profile, too. This, by evaluating a water volume fraction which decreases as one moves further away from the weir.

3.3 | Oscillating basin

With regard to the non-breaking waves, in this section an oscillating basin test is considered. In the case in which a relatively large ratio of total depth h to the wave length λ is assumed, the hydrostatic pressure assumption no longer holds

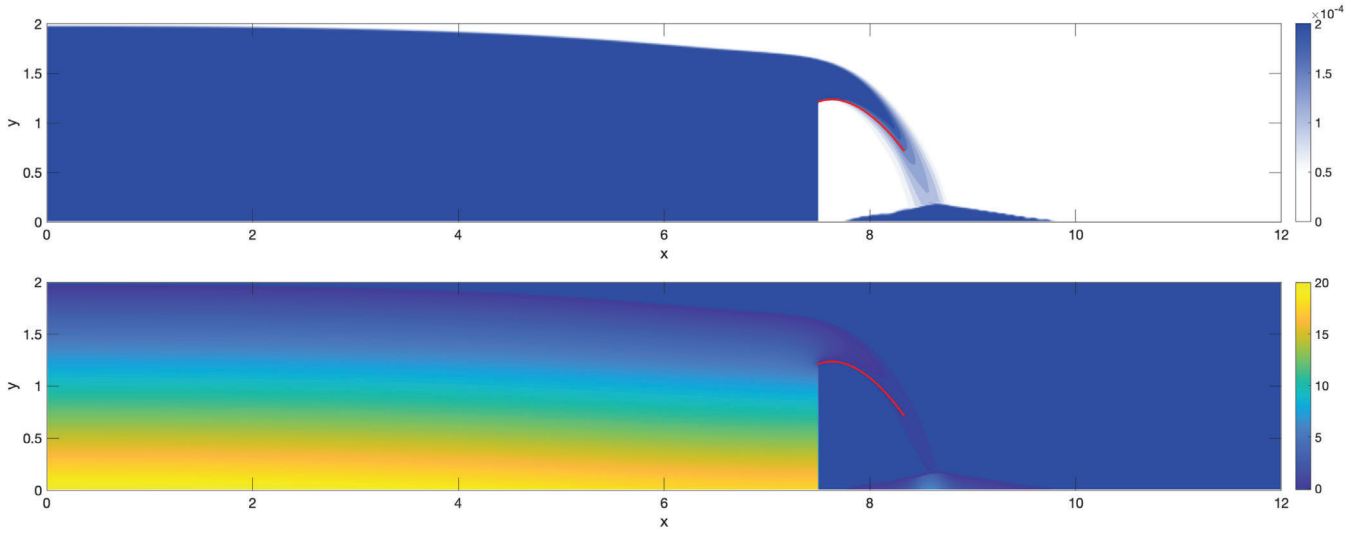

FIGURE 10 Numerical solutions for free surface profile and pressure field, evaluated with the 2D non-hydrostatic conservative methods for the flow over a sharp weir, at time $t = 1.0$. In the first row, the volume fraction (density contours) is represented. In the second row, pressure field is depicted [Colour figure can be viewed at wileyonlinelibrary.com]

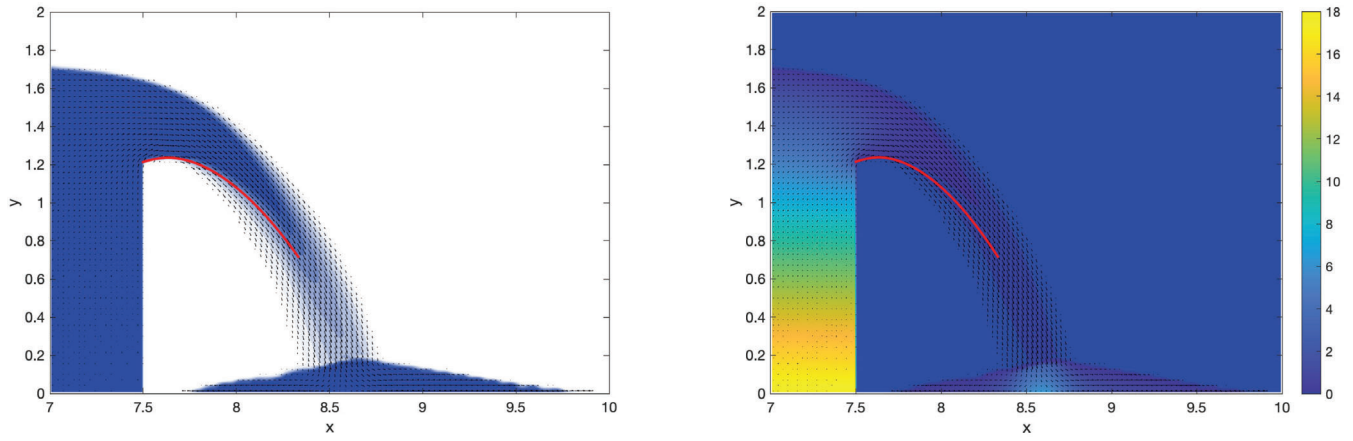

FIGURE 11 Zoom into the flow over a weir. Volume fraction (left) and pressure field (right). The velocity field and the experimental profile found by Scimemi (red solid line) are also shown [Colour figure can be viewed at wileyonlinelibrary.com]

true. Furthermore for small wave amplitude, the wave celerity c is approximated by the following dispersion relation:

$$c = \sqrt{\frac{g\lambda}{2\pi} tanh\left(\frac{2\pi h}{\lambda}\right)}. \tag{42}$$

The computational domain is $\Omega = [-5; 5] \times [0; 10.5]$. The fluid is initially at rest and it is confined in both the left and right parts of the domain, the flow is driven by an initial free-surface of constant slope $h = 10 + 0.01x$. The pressure is set in order to get an initial hydrostatic pressure profile. Wall friction and fluid viscosity are neglected, and the gravity is assumed to be constant and equal to $g = 9.81$. The domain is covered by a uniform grid consisting of 7500 cells, with mesh spacing $\Delta x = 0.1$ in the x-direction and $\Delta y = 0.14$ in the y-direction. The computation is carried out using a Courant–Friedrichs–Lewy number of CFL $= 0.9$ until the final time $t_{end} = 0.5\lambda/c$.

Defining $L = 10$ equal to the domain length in x-direction, the solution consists of a standing wave of length $\lambda = 2L$ and frequency $f = c/\lambda$. In order to compare the analytical and numerical solution more easily, it is useful to define a height coefficient c_h, which can be defined as follows, knowing the initial maximum free surface perturbation $h_{max} = 0.05$ and

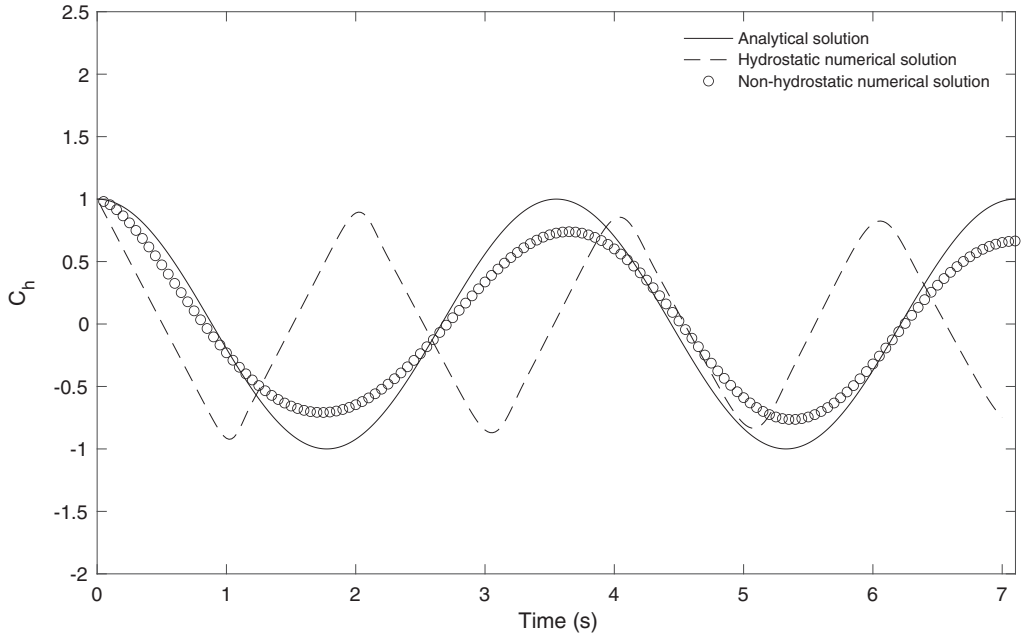

FIGURE 12 Water surface elevations in terms of height coefficient c_h in time. Exact solution (solid line) and numerical solutions with hydrostatic pressure assumption (dashed line) and with non-hydrostatic one (circles) are represented

the average height $h_o = 10$:

$$c_h = \frac{h - h_o}{h_{max}}. \tag{43}$$

A quantitative comparison with the analytical solution of the numerical non-hydrostatic result as well as the numerical solutions with hydrostatic pressure assumption is depicted in Figure 12, where the height coefficient c_h has been plotted over the time t. Both numerical solutions are achieved with the non-hydrostatic model presented in this article, taking for the hydrostatic case simply a single layer in the y-direction.

In Figure 12, it is possible to note that the surface elevation has a periodicity with respect to the time t, but the two numerical solutions have different frequencies. It is quite clear how the hydrostatic solution is wrong and thus different from the analytical solution, since in this case the wave celerity c_{hyd} is equal to $\sqrt{gh}$. Then, the celerities, respectively, read $c \simeq 5.58$ for the dispersion relation in (42) and $c_h \simeq 9.90$ for the hydrostatic case. This explains the two different frequencies that are shown by the numerical results in Figure 12. The results clearly show that the frequency computed with the non-hydrostatic model is in good agreement with the analytical solution which is approximated by the dispersion relation in (42).

3.4 | Smooth flow over a bottom variation

To achieve a second-order convergence, a smooth flow over a bottom variation is considered. It is necessary that this flow represent a stationary problem, due to the fact that a flux-vector splitting scheme is used in the numerical method. Furthermore, the discrete formulation is centered for pressure terms, then for a stationary problem in which momentum is constant in x, the method has to be accurate up to the second order.

The governing differential equation for a stationary shallow-water problem reads:

$$\frac{\partial (hu)}{\partial x} = 0, \tag{44}$$

$$\frac{\partial (hu^2)}{\partial x} + gh\left(\frac{\partial h}{\partial x} + \frac{\partial b}{\partial x}\right) = 0, \tag{45}$$

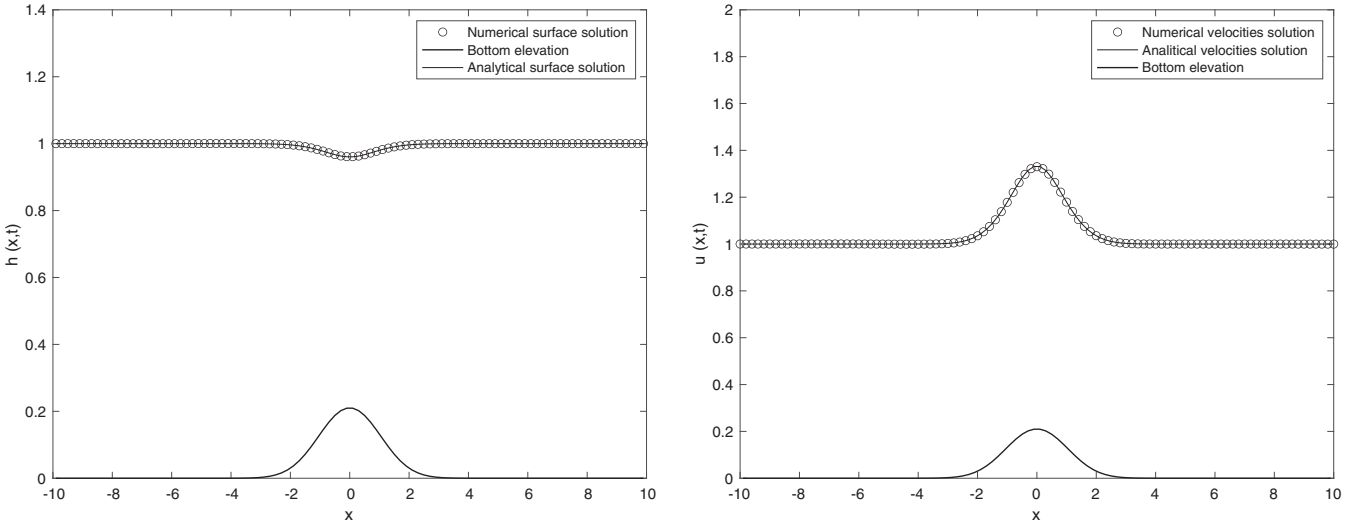

FIGURE 13 The stationary solution of a smooth flow over a bottom variation. Analytical (solid lines) and numerical (circle) solution for the free surface (left) and for the velocity field (right), at time $t = 3.0$

k	Δx_k	N_d	L^2	O_{L^2}
1	0.1	100	7.8701e-04	
2	0.05	200	2.0436e-04	1.95
3	0.025	400	5.2072e-05	1.97
4	0.0125	800	1.3220e-05	1.98

TABLE 2 k-number of the test, mesh size Δx_k, number of elements N_d, L^2-error norm, and numerical convergence rates O_{L^2}, applied to the stationary problem

where $h(x)$ is the free surface height over the bottom, $u(x)$ is the velocity component in the horizontal x direction, $b(x)$ is the bottom elevation, and g is the gravity acceleration. By imposing a smooth perturbation of the free surface $h(x)$ as follows:

$$h(x) = 1 - \frac{1}{4} e^{-\frac{1}{2}x^2}, \tag{46}$$

it is possible to evaluate the variation of the bottom which generates this perturbation of the free surface as a stationary solution. Thus the bottom elevation $b(x)$ yields:

$$b(x) = 1 + \frac{1}{2}\frac{q_o^2}{g} - \frac{1}{2}\frac{q_o^2}{g h(x)^2} - h(x), \tag{47}$$

where q_o is the initial momentum at $t = 0$, which is constant in time. In Figure 13, these two analytical solution are represented by solid lines.

To solve this test case numerically, the full Navier–Stokes method is used but only one discrete cell is assumed in the vertical direction to return to a one-dimensional case, and then the stationary shallow-water problem is solved.

This test case is defined over a fixed spatial domain $\Omega = [-10; 10]$, where continuous exact solutions (47) are discretized according to the mesh adopted. In this way, the stationary analytical solutions provide the initial conditions for h, u over the discrete domain.

Since the exact value for h or for u is known, the standard way to get a precise number for the order of accuracy is to halve the mesh spacing and to look at the ratio of the errors. In Table 2, the k-tests are listed that are carried up, specifying for the sequence the mesh size Δx_k and the number of elements N_d. The momentum is set to be constant in x and equal to $q_o = 1$, wall friction and fluid viscosity are neglected, and the gravity is assumed to be equal to $g = 9.81$. The domain at the boundaries is not closed, at $x = -10$ there is an inflow and at $x = 10$ an outflow, respectively, $q_{oL} = q_{oR} = q_o$ are

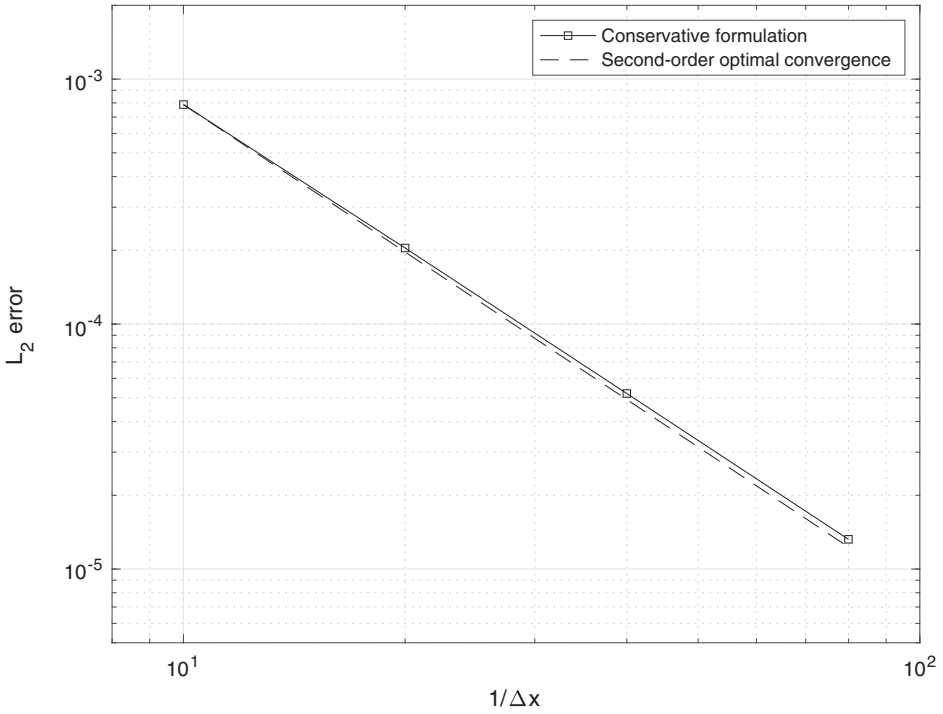

FIGURE 14 L_2-norm error against reciprocal of mesh size. The dashed line shows the theoretical second-order for comparison

imposed. The simulations are carried out using a CFL number of CFL = 0.9, based on the maximum eigenvalue of the system, until the final time $t_{end} = 3$.

The computational results for the coarsest mesh, at the final time $t_{end} = 3.0$, for free surface $h(x)$ and velocity $u(x)$ over the bottom profile $b(x)$, are depicted in Figure 13. It is quite clear that the numerical solution preserves the initial steady state even up to the final time. Since the mesh spacing for the sequence is denoted by Δx_k, the numerical convergence rate O_{L^2} for the L^2 error norm can be computed as

$$\log\left(\frac{L^2_{k-1}}{L^2_k}\right) / \log\left(\frac{\Delta x_{k-1}}{\Delta x_k}\right) = \mathcal{O}(L^2_k). \tag{48}$$

In Figure 14, the L^2-error norm is represented graphically against the number of elements of the mesh with respect to the optimal second-order convergence. The fourth column of Table 2 shows the L^2_k-error norm and the last column contains the corresponding computed convergence rates $\mathcal{O}(L^2)$. As expected, for this steady problem, our mass and momentum conservative scheme converges to the exact solution up to the second order of accuracy.

3.5 | Flow past a circular cylinder in two dimensions

In this section, the steady-state flow past a circular cylinder in two dimensions is considered, as if the $x - y$ plane is orthogonal to the gravity. The computational domain adopted is a square $\Omega = [-5; 5] \times [-5; 5]$, and in the center the circular section of the cylinder with radius $R = 1$ is located. The fluid in the domain is initially at rest, so velocities are imposed equal to zero $u = v = 0$ and the pressure is set uniformly equal to an external reference value $p_{out} = 10\beta$, where β is $\beta = g\frac{\Delta y}{2}$ as defined in Section 2.2. The incoming flow is parallel to the x-axis and it is flowing from the leftmost boundary wall with velocity $u_\infty = 8 \times 10^{-7}$. For such a configuration and flow regime, the potential flow approximation is valid and therefore it provides a reference solution. The analytical solution for this potential flow is obtained easily in polar coordinates r and θ. The velocity components in polar coordinates v_r, v_θ, pressure field p, and the pressure coefficient c_p of the potential flow are given analytically by:

$$v_r = u_\infty\left(1 - \frac{R^2}{r^2}\right)\cos\theta, \qquad v_\theta = -u_\infty\left(1 + \frac{R^2}{r^2}\right)\sin\theta, \qquad p = \frac{1}{2}\rho(u_\infty^2 - v^2) + p_\infty, \qquad c_p = \frac{p - p_\infty}{\frac{1}{2}\rho u_\infty^2}, \tag{49}$$

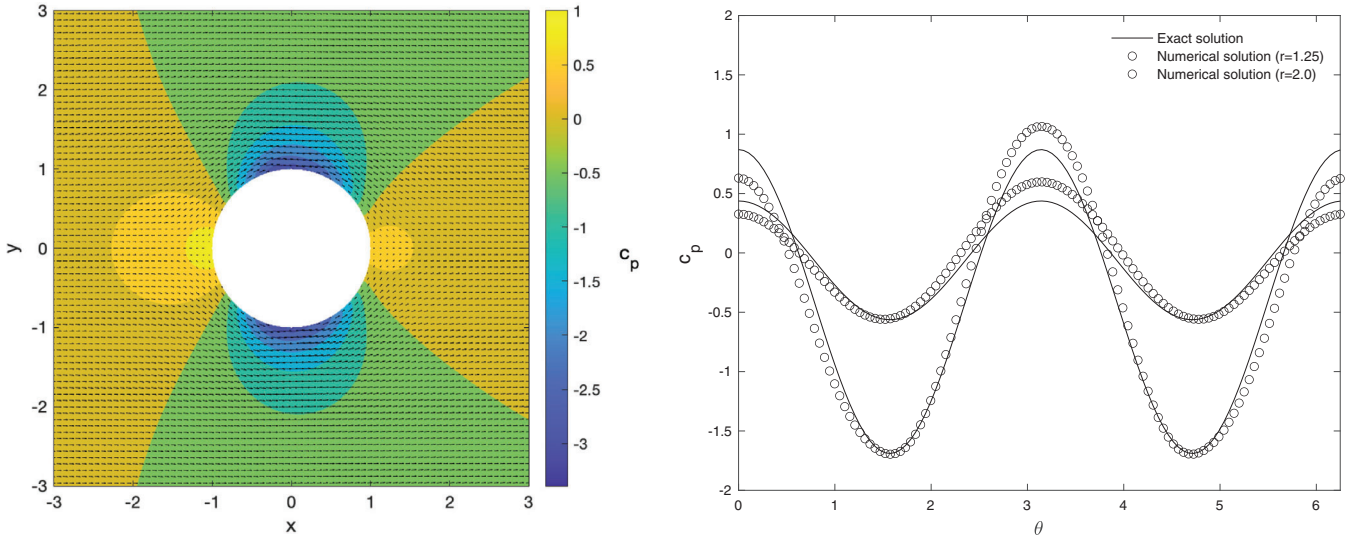

FIGURE 15 The velocities field and c_p distribution for the flow past a circular cylinder evaluated with the 2D non-hydrostatic conservative methods (left) and comparison of c_p with the analytical potential flow solution (right) [Colour figure can be viewed at wileyonlinelibrary.com]

where v^2 is $v^2 = v_r^2 + v_\theta^2$. The computational domain is covered by a uniform rectangular grid consisting of 1.96×10^6 cells, with mesh spacing $\Delta x = 0.00714$ in the x-direction and $\Delta y = 0.00714$ in the y-direction. The cylinder is immersed in the domain by setting the solid volume fraction inside the cylinder to $\alpha_s = 1$, which means that this area cannot be occupied by the fluid. The computation was performed for 2×10^5 time-steps, with a fixed time-step $dt = 2.0$, up to the final time of $t = 4 \times 10^5$. The resulting velocity field together with the c_p distribution as well as a quantitative comparison with the potential flow model is depicted in Figure 15. On the right, the pressure coefficient c_p has been plotted over the azimuthal angle θ for two concentric circles with radii $r = 1.25$ and $r = 2$. The potential flow solution is depicted with the black solid line, it is symmetric with respect to the coordinate axes and has two minimum and two maximum points. The numerical simulation respects this symmetry very well with respect to the x axis, but with respect to the y axis the numerical solution is not symmetric, in particular the second stagnation point results underresolved. This disagreement with the reference solution is most likely due to the numerical viscosity in the scheme and due to the staircase representation of the solid obstacle. Note that usually high order finite volume schemes on unstructured meshes with polynomial reconstruction on boundary interfaces are needed to improve the quality of the numerical results.

4 | CONCLUSIONS

In this article, a new efficient momentum-conservative extension of the semi-implicit mass-conservative scheme presented by Casulli[1] is proposed. The domain is covered by the fluid and by the surrounding void via scalar volume fraction functions for each phase, according to the so-called diffuse interface approach. The particular discretization on a staggered grid allows to reduce the problem to the solution of a mildly nonlinear system for the fluid pressure, which can be efficiently solved by a Newton-type technique. The diagonal nonlinearity stems from the piecewise linear definition of the volume, while the remaining linear part of the system is symmetric and at least positive semi-definite. In a fully implicit formulation, a simple *Picard iteration* technique has to be adopted in order to make again explicit the unknown edge-averaged volume fractions. Once the pressure is known at the new time level, the momentum can be readily obtained via a conservative update formula, which allows the subsequent calculation of the corresponding velocity field.

The stability condition, followed by the time step is only limited by a mild CFL condition based on the flow speed and on the velocity of the moving structures; yet, it is not affected by the gravity wave speed, thus rendering the method efficient for *low Froude number* flows, too.

In terms of accuracy, the choice to use a fully implicit discretization to approximate the pressure gradient and the velocities in the momentum and the continuity equations yields a numerical scheme whose time step is only limited by the flow velocity, instead of the gravity wave speed. However, excessive wave damping may result. To reduce this effect,

the numerical scheme has been extended to up to second order of accuracy in time by introducing the θ-method, where θ is an implicitness parameter in the range $\frac{1}{2} \leq \theta \leq 1$. To further improve the accuracy the advective terms can be calculated using a second order MUSCL-Hancock method.

A thorough validation of one-dimensional inviscid flows has been presented. For one single vertical layer, the two-dimensional method automatically simplifies to a consistent mass and momentum conservative discretization of the hydrostatic one-dimensional shallow water equations. With this simplification the method was used to solve some 1D Riemann problems, for which the exact solution of the shallow water equations is known.

Then the new model has been applied to a set of dambreak problems where the non-hydrostatic behavior is preserved. To achieve this, it is enough to take multiple vertical layers. For these tests, the free surface profile has been compared against analytical and numerical reference solutions. At early times, the vertical acceleration, as well as the pressure gradient in the vertical direction, are the main component of the flow, and thus the hydrostatic pressure assumption of the shallow water model is not verified. The non-hydrostatic results obtained with our new method are in good agreement with the previous results shown in References 30, 34, and 45.

In the last computational examples, it has been shown how this new semi-implicit scheme can be easily extended to simple multi-phase flows, via the use of two different scalar volume fraction functions for water and fixed solid bodies.

Future work will consist in an extension to three space dimensions. In order to improve the computational efficiency, it is possible to proceed with a parallel implementation based on domain decomposition. In future developments, we plan to extend the model by adding the dynamics of a surrounding weakly compressible gas, see, for example, Reference 13, in order to obtain a three-phase flow model which can contain incompressible liquids, rigid and moving solids and a weakly compressible gas phase in the same simulation. Thus, this method may become the basis of a multi-scale and multi-physics model whose applicability ranges from non-hydrostatic multi-valued free surface flows with solid bodies interaction to large scale geophysical flows.

ACKNOWLEDGMENTS

This research was funded by the Italian Ministry of Education, University and Research (MIUR) in the frame of the Departments of Excellence Initiative 2018–2022 attributed to DICAM of the University of Trento (grant L. 232/2016) and in the frame of the PRIN 2017 project *Innovative numerical methods for evolutionary partial differential equations and applications*. M.D. is member of the INdAM GNCS group.

DATA AVAILABILITY STATEMENT

The data that support the findings of this study are available from the corresponding author upon reasonable request.

ORCID


Michael Dumbser https://orcid.org/0000-0002-8201-8372

REFERENCES

1. Casulli V. A semi-implicit numerical method for the free-surface Navier–Stokes equations. *Int J Numer Methods Fluids*. 2014;74:605-622.
2. Klainermann S, Majda A. Compressible and incompressible fluids. *Commun Pure Appl Math*. 1982;35:629-651.
3. Harlow FH, Welch JE. Numerical calculation of time-dependent viscous incompressible flow of fluid with a free surface. *Phys Fluids*. 1965;8:2182-2189.
4. Patankar VS, Spalding B. A calculation procedure for heat, mass and momentum transfer in three-dimensional parabolic flows. *Int J Heat Mass Transf*. 1972;15:1787-1806.
5. van Kan J. A second-order accurate pressure correction method for viscous incompressible flow. *SIAM J Sci Stat Comput*. 1986;7:870-891.
6. Park JH, Munz CD. Multiple pressure variables methods for fluid flow at all Mach numbers. *Int J Numer Methods Fluids*. 2005;49:905-931.
7. Bell JB, Colella P, Glaz HM. A second–order projection method for the incompressible Navier–Stokes Equations. *J Comput Phys*. 1989;85:257-283.
8. Fambri F, Dumbser M. Spectral semi-implicit and space-time discontinuous Galerkin methods for the incompressible Navier-Stokes equations on staggered Cartesian grids. *Appl Numer Math*. 2016;110:41-74.
9. Tavelli M, Dumbser M. A staggered space-time discontinuous Galerkin method for the three-dimensional incompressible Navier-Stokes equations on unstructured tetrahedral meshes. *J Comput Phys*. 2016;319:294-323.
10. Busto S, Ferrín JL, Toro EF, Vázquez-Cendón ME. A projection hybrid high order finite volume/finite element method for incompressible turbulent flows. *J Comput Phys*. 2018;353:169-192.
11. Busto S, Stabile G, Rozza G, Vázquez-Cendón ME. POD–Galerkin reduced order methods for combined Navier–Stokes transport equations based on a hybrid FV–FE solver. *Computers and Mathematics with Applications*. 2020;79:256-273.

12. Busto S, Tavelli M, Boscheri W, Dumbser M. Efficient high order accurate staggered semi-implicit discontinuous Galerkin methods for natural convection problems. *Comput Fluids*. 2020;198:104399.
13. Bermúdez A, Busto S, Dumbser M, Ferrín JL, Saavedra L, Vázquez-Cendón ME. A staggered semi-implicit hybrid FV/FE projection method for weakly compressible flows. *J Comput Phys*. 2020;421:109743.
14. Boscarino S, Russo G, Scandurra L. All Mach number second order semi-implicit scheme for the Euler equations of gasdynamics. *J Sci Comput*. 2018;77:850-884.
15. Munz CD, Roller S, Klein R, Geratz KJ. The extension of incompressible flow solvers to the weakly compressible regime. *Comput Fluids*. 2003;32:173-196.
16. Madsen PA, Murray R, Sørensen OR. A new form of the Boussinesq equations with improved linear dispersion characteristics. *Coast Eng*. 1991;15:371-388.
17. Madsen PA, Sørensen OR. A new form of the Boussinesq equations with improved linear dispersion characteristics. Part 2. a slowly varying bathymetry. *Coast Eng*. 1992;18:183-204.
18. Eskilsson C, Sherwin SJ. An unstructured spectral/hp element model for enhanced Boussinesq-type equations. *Coast Eng*. 2006;53:947-963.
19. Eskilsson C, Sherwin SJ. Spectral/hp discontinuous Galerkin methods for modelling 2D Boussinesq equations. *J Comput Phys*. 2006;212:566-589.
20. Bristeau MO, Mangeney A, Sainte-Marie J, Seguin N. An energy-consistent depth-averaged Euler system: derivation and properties. *Discrete Contin Dyn Syst Ser B*. 2015;20:961-988.
21. Ricchiuto M, Filippini AG. Upwind residual discretization of enhanced Boussinesq equations for wave propagation over complex bathymetries. *J Comput Phys*. 2014;271:306-341.
22. Escalante C, Dumbser M, Castro MJ. An efficient hyperbolic relaxation system for dispersive non-hydrostatic water waves and its solution with high order discontinuous Galerkin schemes. *J Comput Phys*. 2019;394:385-416.
23. Escalante C, Morales T. A general non-hydrostatic hyperbolic formulation for Boussinesq dispersive shallow flows and its numerical approximation. *J Sci Comput*. 2020;83:62.
24. Bassi C, Bonaventura L, Busto S, Dumbser M. A hyperbolic reformulation of the Serre-Green-Naghdi model for general bottom topographies. *Comput Fluids*. 2020;212:104716.
25. Bassi C, Busto S, Dumbser M. High order ADER-DG schemes for the simulation of linear seismic waves induced by nonlinear dispersive free-surface water waves. *Appl Numer Math*. 2020;158:236-263.
26. Favrie N, Gavrilyuk S. A rapid numerical method for solving Serre-Green-Naghdi equations describing long free surface gravity waves. *Nonlinearity*. 2017;30:2718-2736.
27. Busto S, Dumbser M, Escalante C, Favrie N, Gavrilyuk S. On high order ADER discontinuous Galerkin schemes for first order hyperbolic reformulations of nonlinear dispersive systems. *J Sci Comput*. 2021;87:48.
28. Brugnano L, Casulli V. Iterative solution of piecewise linear systems. *SIAM J Sci Comput*. 2007;30:463-472.
29. Brugnano L, Casulli V. Iterative solution of piecewise linear systems and applications to flows in porous media. *SIAM J Sci Comput*. 2009;31:1858-1873.
30. Dumbser M. A simple two-phase method for the simulation of complex free surface flows. *Comput Methods Appl Mech Eng*. 2011;200:1204-1219.
31. Favrie N, Gavrilyuk SL. Diffuse interface model for compressible fluid - compressible elastic-plastic solid interaction. *J Comput Phys*. 2012;231:2695-2723.
32. Ndanou S, Favrie N, Gavrilyuk S. Multi-solid and multi-fluid diffuse interface model: applications to dynamic fracture and fragmentation. *J Comput Phys*. 2015;295:523-555.
33. Favrie N, Gavrilyuk SL, Saurel R. Solid–fluid diffuse interface model in cases of extreme deformations. *J Comput Phys*. 2009;228:6037-6077.
34. Gaburro E, Castro M, Dumbser M. A well balanced diffuse interface method for complex nonhydrostatic free surface flows. *Comput Fluids*. 2018;175:180-198.
35. Busto S, Chiocchetti S, Dumbser M, Gaburro E, Peshkov I. High order ADER schemes for continuum mechanics. *Front Phys*. 2020;8:32. https://doi.org/10.3389/fphy.2020.00032
36. Kemm F, Gaburro E, Thein F, Dumbser M. A simple diffuse interface approach for compressible flows around moving solids of arbitrary shape based on a reduced Baer-Nunziato model. *Comput Fluids*. 2020;204:104536.
37. Toro EF, Vázquez-Cendón ME. Flux splitting schemes for the Euler equations. *Comput Fluids*. 2012;70:1-12.
38. Toro EF. *Riemann Solvers and Numerical Methods for Fluid Dynamics*. 3rd ed. New York, NY: Springer; 2009.
39. Casulli V, Zanolli P. A nested Newton-type algorithm for finite volume methods solving Richards' equation in mixed form. *SIAM J Sci Comput*. 2009;32:2255-2273.
40. Casulli V, Zanolli P. Iterative solutions of mildly nonlinear systems. *J Comput Appl Math*. 2012;236:3937-3947.
41. Casulli V, Cattani E. Stability, accuracy and efficiency of a semi-implicit method for three-dimensional shallow water flow. *Comput Math Appl*. 1994;27:99-112.
42. Toro EF. *Shock-Capturing Methods for Free-Surface Shallow Flows*. Hoboken, NJ: Wiley; 2001.
43. Stansby PK, Chegini A, Barnes TCD. The initial stages of dam-break flow. *J Fluid Mech*. 1998;374:407-427.
44. Ritter A. Die Fortpflanzung von Wasserwellen. *Zeitschrift Verein Deutscher Ingenieure*. 1892;36:947-954.
45. Ferrari A, Dumbser M, Toro EF, Armanini A. A new 3D parallel SPH scheme for free surface flows. *Comput Fluids*. 2009;38:1203-1217.
46. Janosi IM, Jan D, Szabo KG, Tel T. Turbulent drag reduction in dam-break flows. *Exp Fluids*. 2004;37:219-229.

47. Ferrari A, Dumbser M, Toro EF, Armanini A. A new stable version of the SPH method in Lagrangian coordinates. *Commun Comput Phys*. 2008;4:378-404.
48. Scimemi E. Sulla forma delle vene tracimanti - the form of the flow over weirs. *L'Energia Elettrica Milano*. 1930;7(4):293-305.
49. Ferrari A. SPH simulation of free surface flow over a sharp-crested weir. *Adv Water Resour*. 2010;33:270-276.

How to cite this article: Ferrari D, Dumbser M. A mass and momentum-conservative semi-implicit finite volume scheme for complex non-hydrostatic free surface flows. *Int J Numer Meth Fluids*. 2021;93:2946–2967. https://doi.org/10.1002/fld.5017